Key Points:
- Measurement of magnetospheric H^+ and O^+ is critical for understanding dynamics and energization processes
- A novel application of ultrathin foils enables low-resource detection of magnetospheric H^+ and O^+
- Three implementation schemes of this low-resource measurement technique are presented, with one scheme already successfully on-orbit

Correspondence to:
P. A. Fernandes,
pfernandes@lanl.gov

Low-Resource Technique for Measurement of H^+ and O^+ in the Terrestrial Magnetosphere

P. A. Fernandes[1] ⓘD, H. O. Funsten[1] ⓘD, E. E. Dors[1], R. W. Harper[1], B. A. Larsen[1] ⓘD, E. A. MacDonald[2] ⓘD, D. B. Reisenfeld[1] ⓘD, R. M. Skoug[1] ⓘD, J. T. Steinberg[1] ⓘD, and M. F. Thomsen[3] ⓘD

[1]Los Alamos National Laboratory, Los Alamos, NM, USA, [2]NASA Goddard Space Flight Center, Greenbelt, MD, USA, [3]Planetary Science Institute, Tucson, AZ, USA

Abstract Measurement of O^+ in the Earth's magnetosphere is important for monitoring and understanding the initiation and evolution of geomagnetic activity. During active times, O^+ can be the most abundant ion in the magnetosphere. Furthermore, because O^+ and H^+ damage exposed spacecraft materials through different processes, measurement and prediction of O^+ and H^+ fluxes is critical for understanding cumulative damage effects to these materials resulting from the ambient plasma environment of a spacecraft. We describe a simple technique for quantitative, in situ measurement of O^+ and H^+ fluxes using ultrathin foils. This technique is a low-resource addition to a standard electrostatic energy-per-charge analyzer followed by an array of detectors. H^+ and O^+ abundances up to a few tens of keV can be determined by comparison of counts in detectors having no ultrathin foil at the detector aperture, in which both H^+ and O^+ are detected, and adjacent detectors having a foil over the aperture of the appropriate thickness to stop the transmission of O^+ but through which H^+ can transit. We describe three techniques for implementing this method enabling differentiation of O^+ and H^+ in an instrument package significantly simpler than traditional mass spectrometers.

Plain Language Summary Measurement of oxygen ions in near-Earth space is important for monitoring and understanding the current state of the magnetosphere. While hydrogen is typically the most abundant ion in the magnetosphere, during times of enhanced geomagnetic activity oxygen can dominate. Additionally, oxygen and hydrogen ions can damage exposed spacecraft materials by species-dependent processes. Thus, measurement and prediction of oxygen and hydrogen fluxes is critical for understanding cumulative damage effects to spacecraft materials as well as determining magnetospheric activity levels. We describe a simple, low-resource technique for measuring oxygen and hydrogen fluxes in the spacecraft's local plasma environment. This concept utilizes standard measurement techniques for energy selection followed by an array of detectors. The concept uses two types of detectors: one covered with an ultrathin foil and one with no foil. The detector with the foil will measure hydrogen only, as the foil is specifically tuned to prevent oxygen transmission. The detector with no foil measures both oxygen and hydrogen. The abundances of oxygen and hydrogen can be determined by comparison of counts in the two detector types. We describe three techniques for implementing this method enabling differentiation of oxygen and hydrogen in an instrument package significantly simpler than traditional mass spectrometers.

1. Introduction

While H^+ is ubiquitous in the Earth's magnetosphere, early observations of plasma composition indicated the presence of heavy ions (Shelley et al., 1972). Of these heavy ions, the CNO group, often identified simply as O^+, is generally the most abundant, followed by He^+ (Denton et al., 2017; Fernandes et al., 2017; Jahn et al., 2017; Lennartsson, 1989; Lennartsson et al., 1979, 1981) and trace amounts of He^{++} (Gloeckler & Hamilton, 1987; Young et al., 1977, 1982) and molecular ions (Craven et al., 1985; Seki et al., 2019). O^+ predominantly originates from the ionosphere, where it can be energized, resulting in outflow to the magnetosphere (Chappell et al., 1987; Shelley et al., 1972). Generally, O^+ is more abundant nearer the Earth than at larger radial distances (Maggiolo & Kistler, 2014; Mouikis et al., 2010; Young et al., 1982).

Measurement of the phase space distribution of O^+ provides insight into the complex dynamics of an energized magnetosphere and can be used to monitor space weather. Magnetospheric oxygen abundance is correlated with solar activity due to enhanced sourcing of heavy ions by the ionosphere during active solar times (e.g., Kistler & Mouikis, 2016; Young et al., 1982). Likewise, during periods of strong geomagnetic activity O^+ fluxes typically increase at all L-shells and magnetic local times (Balsiger, 1981; Denton et al., 2005, 2017; Fernandes et al., 2017; Fu et al., 2001; Geiss et al., 1979; Gloeckler & Hamilton, 1987; Jahn et al., 2017; Johnson, 1979; Johnson et al., 1975; Kistler & Mouikis, 2016; Lennartsson et al., 1981; Lennartsson & Sharp, 1982; Maggiolo & Kistler, 2014; Shelley et al., 1972; Young, 1983; Young et al., 1982). O^+ is a major contributor to the ring current, the population of particles that carries a large fraction of the energy density in the inner magnetosphere (Kistler et al., 2016). Intensifications in the ring current are observed as a significant decrease in Earth's surface magnetic field—this criterion defines the onset of a geomagnetic storm. O^+ can become the dominant species of the storm time ring current (Hamilton et al., 1988), making it an excellent proxy for evaluating space weather disturbances. O^+ also plays an important role in reconnection and influences the onset of geomagnetic substorms (Karimabadi et al., 2011; Kistler et al., 2005; Kronberg et al., 2014; Wygant et al., 2005).

In addition to providing insight into disturbances in the geospace environment, measuring oxygen in near-Earth space is critical for satellite safety and operations due to its ability to cause significant damage to the spacecraft. At energies of tens of keV, O^+ is capable of causing more damage than H^+ due to its larger mass and high reactivity. For ion energies below 50 keV, H^+ loses most of its energy to excitations and ionizations of electrons in the target material (e.g., 94% for 10 keV H^+ incident on silicon (Funsten et al., 2004)). While this energy loss process cannot damage conductors or semiconductors, it can cause dielectric material charging resulting in damaging electrostatic discharges as well as chemical modification of the material (Marletta & Iacona, 1993; see also review by Plis et al., 2019, and references therein). However, O^+ loses a significant amount of its incident energy to Coulombic interactions with atoms in the material (e.g., 66% for 10 keV O^+ incident on silicon (Funsten et al., 2004)). This can cause a high density of atomic displacements and rearrangement along the ion track in both dielectric and conductive materials, resulting in chemical and physical modification of the material structure.

The capacity for damage from incident oxygen has been the impetus for targeted flight experiments, including the Evaluation of Oxygen Interaction with Materials III (EOIM-III) flight experiment (Roussel & Bourdon, 2000) and the Long Duration Exposure Facility (LDEF) experiment (Brinza, 1993). Physical modification of spaceflight materials by oxygen include sputtering or abstraction of individual atoms from the target material (Tennyson, 1993), sometimes resulting in degradation of mechanical properties including modulus, strength, and dimensional stability (Brinza, 1993; Koontz et al., 1991). Organics such as polymer films (including polyimides) and polyether ether ketone (PEEK) plastic are especially sensitive to exposure to on-orbit oxygen (Banks et al., 2004). Polyimides in particular are widely used in spacecraft as they are a core constituent of spacecraft multilayer insulators (MLI); exposure to atomic oxygen adversely affects their chemical structure, resulting in surface texturing and erosion of the material (Tahara et al., 1995). Changes in optical properties of materials have also been observed, including severe degradation of optical coatings (Paillous, 1993), fogging of silvered Teflon blankets flown on LDEF (Brinza, 1993), and degradation of solar panel power production (Visentine et al., 2002). Techniques such as employing protective coatings help mitigate the detrimental effects of oxygen (Banks et al., 1993). However, continued monitoring of the in situ hydrogen and oxygen populations is critical for understanding and predicting the impact of the plasma environment on spacecraft materials throughout the magnetosphere.

A variety of mass spectrometers onboard many missions have been flown over the last half-century (for a detailed review see Young, 1998) to study the composition of the terrestrial magnetosphere in order to better understand its structure, dynamics, and coupling to the ionosphere and solar wind. Orthogonal electric and magnetic fields were employed in mass spectrometers on 1971-089A/CXA (Shelley et al., 1972) and CRESS/LOMICS (Collin et al., 1992; Young et al., 1992). A double-focusing spectrometer utilizing crossed cylindrical electric and magnetic fields flew on GEOS/ICE and ISEE-1/PCE (Balsiger et al., 1976; Shelley et al., 1978), and magnetic spectrometer Geotail/CPI employed electromagnets (Frank et al., 1994). Time-of-flight (TOF) mass spectrometers, often leveraging ultrathin carbon foils to help generate start/stop signals, include AMPTE/CCE (Gloeckler et al., 1985), CLUSTER/CIS (Rème et al., 1997), POLAR/TIDE
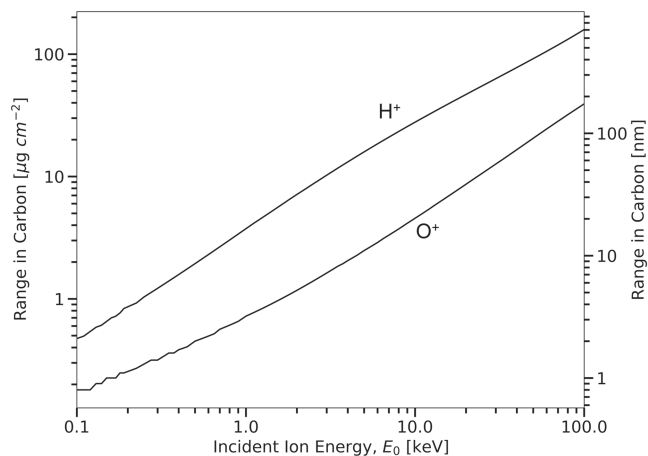
Figure 1. The range of H^+ and O^+ in carbon calculated using the Stopping and Range of Ions in Matter (SRIM) software and shown as a function of incident ion energy E_0. Ranges are shown in $\mu g \cdot cm^{-2}$ (left axis) and nm (right axis) assuming that the foils are 100% pure carbon. At a given energy, the range of H^+ is much greater than that of O^+. Therefore, a wide energy range exists over which O^+ will be stopped in a carbon foil whereas H^+ will be transmitted.

(Moore et al., 1995), FAST/TEAMS (Möbius et al., 2013), Van Allen Probes/HOPE (Funsten et al., 2013; Spence et al., 2013), and MMS/HPCA (Young et al., 2014). When compared with plasma spectrometers with no compositional capability, mass spectrometers usually require significant additional resources. For example, magnetic mass spectrometers are typically heavy, and TOF spectrometers require fast timing circuits, long drift lengths, and often additional high voltages.

New techniques for measuring ion composition focus on decreasing size, weight, and/or power requirements (e.g., MacDonald et al., 2009). Here we describe a low-resource, thin-foil technique to measure H^+ and O^+ fluxes in magnetospheric plasma. Although the mass resolution of this technique is poorer than dedicated magnetic or TOF mass spectrometers and cannot resolve minor species of the magnetosphere, it is sufficient to distinguish the dominant magnetospheric species H^+ from O^+ because of their large mass difference. More specifically, the instrument response to H^+, He^+, and He^{++} will be indistinguishable. Similarly, the instrument cannot distinguish C^+, N^+, and O^+ from each other. These minor species add some additional uncertainty to the measurements which would require quantification in a full instrument build. For this manuscript, we focus on describing the technique, which enables monitoring and assessment of the plasma environment of the spacecraft and provides information about the magnetospheric activity level.

2. Technique for Distinguishing O^+ From H^+

Ultrathin foils are commonly used in space instrumentation in applications ranging from energetic neutral atom (ENA) imagers (e.g., Funsten et al., 2009; McComas et al., 2012; Moore et al., 2000; Pollock et al., 2000) to time-of-flight mass spectrometers (e.g., Allegrini et al., 2016; McComas et al., 2004; Wüest, 1998, and references therein). These instruments exploit several properties of the interaction of fast atoms or molecules with ultrathin foils. When an incident particle traverses an ultrathin foil, (a) the charge state of the incident particle may be modified upon exiting the foil, (b) a secondary electron may be generated on the entrance and/or exit surfaces of the foil, and (c) a molecular ion may be dissociated into its constituent atoms. Particles lose energy and experience angular scattering in the foils; thus, thinner foils are used to minimize these effects (e.g., Allegrini et al., 2014, 2016; Ebert et al., 2014; McComas et al., 2004). The foil stopping power, and thus the ability of a particle to traverse a foil, depends both on incident particle energy and species; we exploit this dependence for a low-resource technique that distinguishes H^+ from O^+ for space weather applications.

We use carbon as the ultrathin foil material because it is easily fabricated, its thickness can be controlled with reasonable accuracy (typically ± 0.5 $\mu g \cdot cm^{-2}$ as cited by the manufacturer), and carbon foils have been successfully used on more than 20 space-based instruments (e.g., Allegrini et al., 2016; McComas et al., 2004; Wüest, 1998, and references therein). These foils are mounted on high-transmission grids that enable large aperture areas and survival of the foils in the harsh vibration and acoustic environment of launch. Figure 1 shows the mean projected range of H^+ and O^+ incident on a carbon target derived using the Stopping and Range of Ions in Matter (SRIM) simulation (Ziegler & Biersack, 1985). For incident ions with energy 0.1–50 keV, the range of H^+ in the carbon target is approximately 4 times the range of O^+. Thus, a carbon foil of specified thickness will transmit H^+ and completely stop O^+ over a predictable energy range. The optimal foil thickness will be selected based on the energy range needed to meet the measurement objectives of the particular mission.

In Figure 2 we present a simple instrument concept for demonstrating the utility of this technique, based on a two-detector configuration (Funsten et al., 2007). This concept uses two electron multiplier detectors, such as a channel electron multiplier (CEM) or microchannel plate (MCP). Detector 1 (D1) lies behind a grid with a thin foil, and detector 2 (D2) lies behind a grid with no foil. Using identical grids helps ensure that D1 and D2 have similar opacity and electric field geometry between the grid and entrance to the electron multiplier
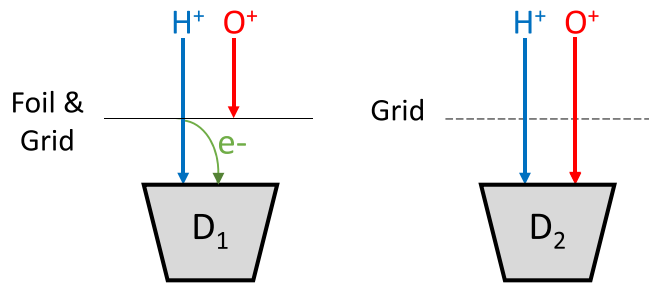
Figure 2. Schematic of a low-resource instrument concept for differentiating H^+ and O^+. Detector D1 consists of a channel electron multiplier (CEM) behind a grid with a foil, whereas detector D2 is a CEM detector behind a grid with no foil. The foil in front of D1 is of such thickness that H^+ is transmitted while O^+ is blocked. The D1 count rate is a measure of the H^+ flux, and the difference in count rates between D1 and D2 is a measure of the O^+ flux.

(Funsten et al., 1996). Although secondary electrons are generated at the entrance and exit surfaces of the foil covering D1, the secondary electron generated on the entrance surface is not detected and therefore not shown in Figure 2. Any secondary electrons generated at the grid with no foil covering D2 are negligible and approximated as zero in this analysis.

An ion that traverses the foil loses an amount of energy that depends on the foil thickness, foil composition, and ion energy and species. By designing the foil to transmit H^+ while stopping O^+ at the same incident energy, D1 detects only H^+, whereas D2 detects both H^+ and O^+. Therefore, comparison of the count rates between D1 and D2 enables quantification of the incident H^+ and O^+ fluxes.

3. Transmission of O^+ and H^+ Through Thin Foils

To evaluate this technique, we measured the transmission of 1–60-keV H^+ and O^+ beams through carbon foils of several different thicknesses. Nominal 1-, 4-, 6-, 8-, 10-, and 12-$\mu g \cdot cm^{-2}$ carbon foils, in which the nominal thickness refers to the foil thickness value cited by the manufacturer, were procured and subsequently mounted on a 333 line-per-inch (lpi) electroformed Ni grid that was affixed to a frame containing a 5.9-mm-diameter aperture. We measured the grid transmission, equivalent to the open area of the grid, to be $T_G = 0.83$. Table 1 summarizes the characteristics of the eight foils used in this experiment.

3.1. Foil Thickness Assessment

Prior to evaluating the proposed technique for differentiating H^+ ions from O^+ ions, the carbon foils must first be characterized to ensure that their performance is consistent with the manufacturer-provided nominal thicknesses. The analysis of Meyer (1971) derived a dependence of the ion energy E_0 on the half-width $\psi_{1/2}$ of the angular scattering distribution, $\psi_{1/2} \propto \frac{1}{E_0}$, for a particular foil composition, thickness, and incident ion species. We exploit this systematic dependence to quantify the performance of the foil using the foil constant k_F, defined as

$$k_F = E_0 \psi_{1/2} \qquad (1)$$

where E_0 is the incident ion energy and $\psi_{1/2}$ is the measured angular scattering half-width at half maximum.

The foils used in this study were evaluated by measuring the angular scatter distribution of H^+ transmitted through the foil and deriving the foil constant, a standard measurement used as a proxy for foil thickness (Funsten et al., 1992, 1994; Funsten, McComas, et al., 1993). The H^+/O^+ separation technique described in section 2 relies on the thickness of the foil and not the angular scattering of ions through the foil; therefore, no measurement of the angular scattering of O^+ through the foil is necessary.

Table 1
Summary of Carbon Foil Thicknesses Used in This Study

	Manufacturer-reported nominal thickness ($\mu g \cdot cm^{-2}$)	Foil constant k_F (keV deg)	Calculated nominal thickness ($\mu g \cdot cm^{-2}$)
Foil 1	1	35	0.83
Foil 2	4	67.8	4.02
Foil 3	6	89.3	6.11
Foil 4	8	107.8	7.90
Foil 5	10	134.2	10.47
Foil 6	12	144	11.42
Foil 7	12	151.2	12.12
Foil 8	10	168.2	13.77

Note. The nominal thickness is provided by the manufacturer. The foil constant is determined experimentally using H^+. The calculated thickness is determined from the experimental results using equation (2).
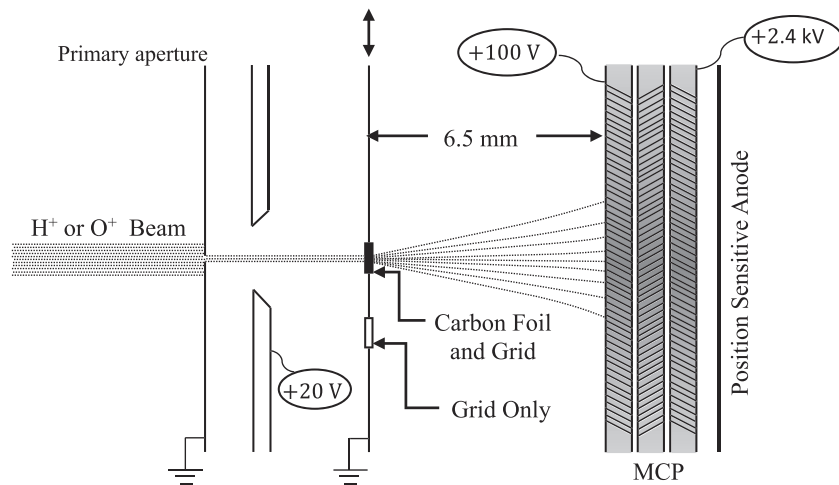
Figure 3. Experimental apparatus used for both characterizing thicknesses of ultrathin foils and for demonstrating the technique for distinguishing H^+ from O^+. The H^+ or O^+ beam enters from the left. The primary aperture defines the beam size, while the secondary aperture is biased to +20 V to collect secondary electrons generated at the primary aperture or the foil/grid. A translational stage enables setup of multiple configurations of foils and grids without needing to break vacuum. After passing through the foil/grid or grid only, the beam is imaged on the microchannel plate (MCP) detector.

The experimental apparatus for characterizing the foils is shown in Figure 3 and uses a Quantar Technology Inc. imaging MCP detector (series 3395). A magnetically mass-resolved collimated beam of H^+ ions of known energy E_0 and constant flux Φ was first directed toward the grounded primary aperture which defined the beam size. For this foil thickness characterization measurement, the primary aperture was 0.2 mm. Immediately following the primary aperture was a 7-mm aperture biased to +20 V to capture any stray secondary electrons generated at the beam-defining primary aperture which could potentially contaminate the flux measurement. This secondary aperture was sufficiently large and its potential was sufficiently low that it did not affect the energy nor spatial distribution of the incident ion beam. Following this pair of apertures, the beam was incident on a frame with support grid and foil. The distance d between the foil and the MCP detector was 6.5 mm. The frame and grid holding the foil were grounded while the front surface of the MCP detector was held at +100 V. Protons traversed the foil and were scattered; proton measurements at the MCP detector enabled calculation of the angular scattering distribution, which is used as a proxy for the foil thickness using the technique described in detail in Funsten et al. (1992).
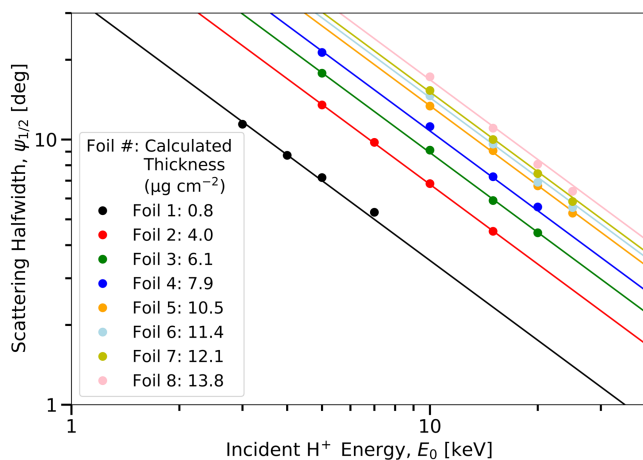
Figure 4 shows the measured angular scattering half-width as a function of incident H^+ energy for the foils used in this study. The foil constants for each foil were derived from a fit of equation (1) to the angular scattering data and are shown as the solid lines of constant k_F in Figure 4. Measured results for Foil 8 were inconsistent with the manufacturer's reported value of 10 $\mu g \cdot cm^{-2}$; measurement indicated Foil 8 has foil constant 168.2 keV·deg, which exceeds that of the 12-$\mu g \cdot cm^{-2}$ foils. Based on the measured k_F, this foil has a thickness that more closely corresponds to a nominal 14-$\mu g \cdot cm^{-2}$ thickness. The thicknesses of other nominal 10-$\mu g \cdot cm^{-2}$ foils from the same procurement lot (not shown in this study) were also consistently measured to a value of k_F that was higher than expected, suggesting a systematic fabrication error of that lot. The other nominal 10-$\mu g \cdot cm^{-2}$ foil shown in Figure 4 was from a different procurement lot and exhibited a foil constant consistent with its nominal thickness. These measurements demonstrate variability relative to manufacturer-reported thicknesses and highlight the importance of evaluating the foils prior to usage in instrumentation.

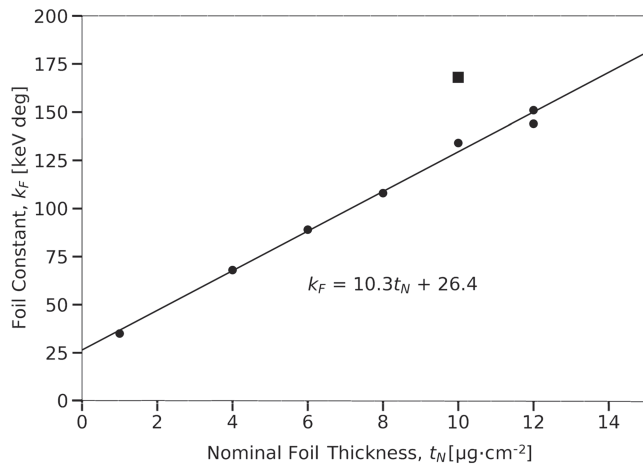**Figure 4.** The measured angular scattering half-width at half maximum of H^+ transmitted through carbon foils of various nominal thickness is shown as a function of the incident ion energy. The lines represent fits to the data using equation (1).

Figure 5. The foil constant k_F, derived by fitting equation (2) to the H$^+$ data in Figure 4, is a measure of the foil thickness and is shown as a function of the manufacturer-reported "nominal" foil thickness. The solid line is a fit to all data except the anomalous square data point (described in detail in the text).

Figure 5 shows the foil constant derived from the H$^+$ data in Figure 4 as a function of the nominal foil thickness. The foil constant k_F (keV·deg) varies linearly with the nominal foil thickness τ_N (µg·cm^{-2}), with the exception of the anomalous 10-µg·cm^{-2} foil represented by the lone square data point. A fit to the data (excluding the square data point) yields

$$k_F = 10.3\tau_N + 26.4. \tag{2}$$

Table 1 summarizes the foil characteristics including tabulation of the reported nominal foil thickness as provided by the manufacturer, the foil constant resulting from the measured scattering half-angle, and the calculated nominal thickness resulting from the fit shown in equation (2). Although k_F was determined from H$^+$ data, this quantity is used as a proxy for foil thickness, an innate characteristic of the foil which is independent of the incident ion species.

Extrapolation of equation (2) to $\tau_N = 0$, which ideally corresponds to a carbon foil of zero thickness, results in a foil constant $k_F = 26.4$ keV·deg, suggesting a systematic, constant-thickness residual layer in addition to the carbon foil. The first term of equation (2) is interpreted as representing the actual thickness of the deposited carbon since the carbon deposition is accurately measured by the manufacturer using a quartz crystal microbalance. The second term represents a residual layer that likely consists of a residual parting agent attached to the carbon layer and/or adsorbates introduced during the foil fabrication or mounting process (Ebert et al., 2014; Funsten et al., 1992; Funsten, McComas, et al., 1993; Funsten & Shappirio, 1997; McComas et al., 2004; Ritzau & Baragiola, 1998). Based on the linear correlation between k_F and τ_N, (i.e., a nominal 1 µg·cm^{-2} foil corresponds to 10.3 keV·deg according to equation (2)), the equivalent carbon thickness of this residual layer is ~2.5 µg·cm^{-2}. We note that carbon foils much thinner than those used in this study typically appear to have a much thinner residual layer than suggested by equation (2). For example, a nominal 0.5-µg·cm^{-2} carbon foil was measured to have a foil constant k_F in the range of 12–15 keV·deg (Funsten, McComas, et al., 1993), and the foil thickness itself is much thinner than the residual layer of ~25 µg·cm^{-2} obtained for the thick foils used here. This variability again emphasizes the need for experimentally characterizing foil thicknesses before implementing them into an instrument.

3.2. Experimental Technique for H$^+$ and O$^+$ Differentiation

The experimental apparatus for demonstrating the low-resource mass separation technique is shown in Figure 3. This setup is identical to the setup described for foil thickness characterization in section 3.1 with one minor change: for demonstrating the low-resource mass separation technique, the primary aperture is 2.7 mm.

The magnetically resolved, collimated beam of H$^+$ or O$^+$ ions was incident on a frame with a support grid only (D2 in Figure 2), and the output count rate C_2 from the MCP detector was measured. The foil-less aperture was then replaced by an aperture frame with a foil and its support grid, representative of D1 in Figure 2, and the count rate C_1 was measured.

For both configurations D1 and D2, the distance d between the grid and the MCP detector was 6.5 mm, and the grid geometry and opacity were identical. The aperture frames and grids of D1 and D2 were grounded while the front surface of the MCP detector was held at +100 V. The potential difference between the foils/grids and the front surface of the MCP maximized the ion detection efficiency and imaging resolution in two ways. First, secondary electrons created by ions or electrons that strike the web region of the front MCP are electrostatically redirected back toward the detector and could thus initiate an electron avalanche in the MCP, ensuring (a) that the incident ions are detected and (b) that they are detected at the correct location on the MCP (Funsten et al., 1996). Second, ions that transit the foil can generate secondary electrons at the exit surface of the foil which are accelerated toward the MCP and similarly enhance the detection probability. Thus, an enhanced detection efficiency results from (a) detection of the ion only, (b) detection of the

secondary electrons off the foil only, or (c) detection of the ion and secondary electrons off the foil registering as a single count. The arrival time difference between an incident ion and the secondary electrons it generates was determined to be ≤ 56 ns for H^+ and O^+ ions spanning 1–50 keV. This is much smaller than the μs deadtime of the Quantar detector system, ensuring that an incident ion and its secondary electrons did not register as two counts.

We define E_0 as the energy of an incident ion at the entrance of the aperture. An incident ion loses energy as it transits the foil. The mean energy loss $\Delta E (\tau_F)$ depends on the thickness of the foil τ_F. We define E_F as the mean energy of an exit distribution of ions after transmission through the foil:

$$E_F(E_0, \tau_F) = E_0 - \Delta E(\tau_F). \tag{3}$$

For the results presented here, E_0 is well-defined by the experimental apparatus. ΔE was not determined because it is not required for determining H^+ and O^+ abundances using the method described.

The count rate $C_{1,j}$ (# s^{-1}) resulting from ions incident on the MCP in configuration D1 is

$$C_{1j}(E_0, \tau_F) = A\Phi_j T_G \varepsilon_{1,j}(E_0, \tau_F) T_{F,j}(E_0, \tau_F) \tag{4}$$

where j denotes the ion species ($j = H^+$ or O^+), A is the area of the detector (cm^2), Φ_j is the collimated monoenergetic flux ($cm^{-2} s^{-1}$) of ion species j at energy E_0 incident on the aperture, T_G is the grid transmission (0.83 for the grids used in this study), $\varepsilon_{1,j}(E_0, \tau_F)$ is the detection efficiency of ions that transit the foil, and $T_{F,j}(E_0, \tau_F)$ is the probability of transmission through the foil for ions of species j. Because secondary electrons from the backside of the foil can be detected in addition to the transmitted incident ion, the detection efficiency of ions that transit the foil is

$$\begin{aligned} \varepsilon_{1,j}(E_0, \tau_F) &= 1 - \left(1 - \varepsilon_{ION,j}(E_F(E_0, \tau_F))\right)\left(1 - \varepsilon_{SE,j}(E_F(E_0, \tau_F))\right) \\ &= \varepsilon_{ION,j}(E_F(E_0, \tau_F)) + \varepsilon_{SE,j}(E_F(E_0, \tau_F)) - \varepsilon_{ION,j}(E_F(E_0, \tau_F))\varepsilon_{SE,j}(E_F(E_0, \tau_F)). \end{aligned} \tag{5}$$

This can be rewritten without explicit dependencies for clarity as

$$\begin{aligned} \varepsilon_{1,j}(E_0, \tau_F) &= 1 - \left(1 - \varepsilon_{ION,j}\right)\left(1 - \varepsilon_{SE,j}\right) \\ &= \varepsilon_{ION,j} + \varepsilon_{ION,j} - \varepsilon_{ION,j}\varepsilon_{SE,j}. \end{aligned} \tag{5b}$$

In equation (5), $\varepsilon_{ION,j}(E_F(E_0, \tau_F))$ is the efficiency that a transmitted ion of species j is detected by the MCP detector. Efficiency $\varepsilon_{SE,j}(E_F(E_0, \tau_F))$ is the detection efficiency of secondary electrons emitted from the exit surface of the foil by the transmitted ion (note that the number of secondary electrons generated and the efficiency of their detection are both contained in ε_{SE}). Both ε_{ION} and ε_{SE} are a function of the energy $E_F(E_0, \tau_F)$ of the ion at the exit surface of the foil, which in turn is a function of the foil thickness and the incident ion energy. The quantity $(1 - \varepsilon_{ION,j})(1 - \varepsilon_{SE,j})$ in equation (5) corresponds to the probability that an ion of species j that transits a foil is not detected either by its impact on the CEM detector or by secondary electrons emitted from the exit surface of the foil which then impact on the detector; this parameterization requires that these probabilities are independent, a reasonable assumption for this configuration.

The count rate $C_{2,j}$ resulting from ions detected in configuration D2, which has no foil, is

$$C_{2,j}(E_0) = A\Phi_j T_G \varepsilon_{2,j}(E_0) \tag{6}$$

where $\varepsilon_{2,j}(E_0)$ is the detection efficiency of ions of species j that are incident on the MCP detector. The grid transmission T_G, detector area A, and the collimated monoenergetic ion beam flux Φ_j for each ion species are assumed to be the same as for configuration D1.

The ratio of count rates from configurations D1 and D2 for a particular ion species j (e.g., j represents H^+ or O^+) at incident energy E_0 is
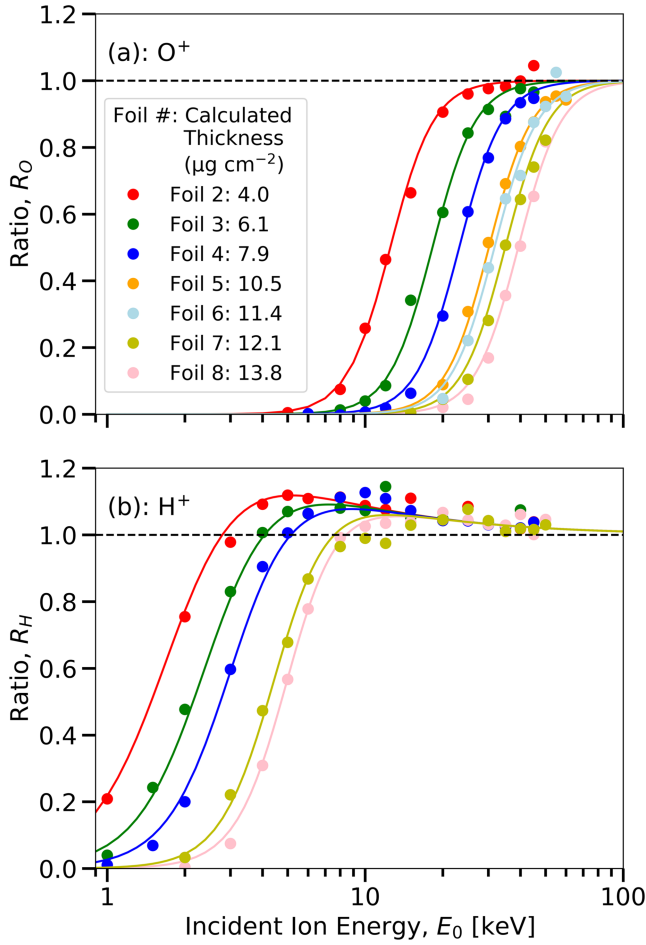
Figure 6. The measured ratios R of counts in detector D1 relative to detector D2 described in equation (7) are shown for incident beams of (a) O^+ and (b) H^+ as a function of incident energy for several different foil thicknesses. The solid lines are fits to the data using (a) equation (8) and (b) equation (10).

$$R_j(E_0, \tau_F) = \frac{C_{1,j}(E_0, \tau_F)}{C_{2,j}(E_0)} = \frac{\varepsilon_{1,j}(E_0, \tau_F)}{\varepsilon_{2,j}(E_0)} T_{F,j}(E_0, \tau_F). \tag{7}$$

For ion species j, the ratio R_j is related to the ion transmission probability $T_{F, j}$ by the ratio of the energy-dependent detection efficiencies $\varepsilon_{1, j}$ and $\varepsilon_{2, j}$. Because MCP and CEM detectors rely on initiation of a secondary electron avalanche by an incident ion in the detector or, for the case of configuration D1, secondary electrons emitted from the exit surface of the foil, the energy dependence of $\varepsilon_{1, j}$ and $\varepsilon_{2, j}$ follows the electronic stopping power curve which generally increases with increasing ion mass and with increasing ion energy over the energy range of ions used here (Ritzau & Baragiola, 1998).

3.3. Detector Response for H^+ and O^+

Figures 6a and 6b show the measured ratios R_H and R_O, respectively, as a function of the incident ion energy E_0 for foils of various thicknesses. Qualitatively, several expected features are apparent for particular combinations of ion species and foil thickness. First, neither H^+ nor O^+ are observed to transit a foil at very low energies because they lose all of their energy and are completely stopped in the foil. Therefore, for measurement of H^+ at these very low energies, the foil must be biased to a voltage V_F so that H^+ will be accelerated to sufficient energy to transit the foil and be detected, while ensuring that the similarly accelerated O^+ does not transit the foil. From Figure 6, an acceleration voltage of $V_F = 8$ kV is suitable. Second, the energy at which ions begin to transit a foil increases with increasing foil thickness. Third, O^+ begins to transit a foil of a particular thickness at an energy that is substantially higher than for H^+ due to the larger energy loss of O^+ in the foil relative to H^+. These three observations are consistent with many previous measurements (e.g., Allegrini et al., 2014; Bürgi et al., 1993; Ebert et al., 2014; Funsten, Barraclough, et al., 1993; Funsten, McComas, et al., 1993). Fourth, the transmission of both H^+ and O^+ at higher energies increases toward a maximum corresponding to $R_j \approx 1$ as more ions successfully transit the foil. R_H actually reaches a value slightly higher than unity and subsequently approaches a value of $R_H = 1$, the reason for which is discussed below. Data for Foil 1 are not shown in Figure 6 because the foil was too thin, enabling near-complete transmission of both species over the energy range. H^+ measurements were not taken for Foils 5 and 7.

The O^+ data were fit to a sigmoid function of the form

$$R_O = \frac{E_0^b}{E_C^b + E_0^b} \tag{8}$$

where E_C, which is a function of the foil thickness, is the energy at which $R_O = 0.5$, and the value of the exponent b governs the rate at which R_O rises from $R_O = 0$ to $R_O = 1$. The value of b was found to be independent of the foil thickness and energy, and the fit resulted in $b = 5.14$ for O^+. The fitted values of E_C for O^+ are shown in Figure 7 as a function of the foil constant k_F. A linear dependence of E_C on k_F is observed; a fit to the O^+ data yields

$$E_C = 0.269 k_F - 5.82 \tag{9}$$

where E_C is in units of keV and k_F is in units of keV·deg.

As observed in Figure 6b, the ratio R_H of count rates for incident H^+ overshoots above a value of unity before converging on unity at higher energies. This was fit to a modified sigmoid function of the form
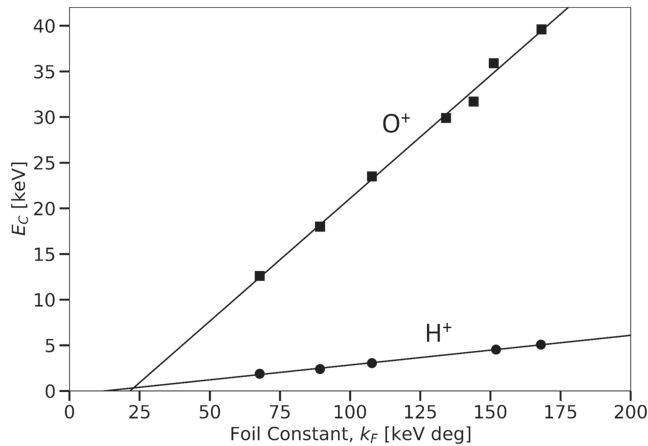
Figure 7. The derived values of the fitting constant E_C, which corresponds to the incident ion energy at which the transmission ratio $R \approx 0.5$, exhibit a linear dependence on the foil constant k_F, which is a measure of the foil thickness determined using protons. The solid lines are linear fits to the derived values of E_C.

$$R_H = \frac{E_0^b}{E_C^b + E_0^b} \left(1 + \frac{1}{1 + aE_0} \right) \tag{10}$$

where the term $(1 + (1 + aE_0)^{-1})$ produces the observed overshoot $R_H > 1$. The parameters a and b were found to be independent of the foil thickness or incident ion energy, and the fit of equation (10) to the H$^+$ data yielded $a = 1.04$ keV^{-1} and $b = 3.69$. Figure 7 shows the values of E_C derived by fitting equation (10) to the H$^+$ transmission data for each of the foils. As with the O$^+$ transmission, a linear dependence of E_C on k_F was observed, and a linear fit to the H$^+$ data resulted in

$$E_C = 0.0325k_F - 0.415 \tag{11}$$

where, as before, E_C is in units of keV and k_F is in units of keV·deg.

The presence of an overshoot of R_H is associated with the detection efficiencies $\varepsilon_{2,H}(E_0)$ and $\varepsilon_{1,H}(E_0, \tau_F)$. For foil thicknesses and ion energies in which the probability of transmission through the foil approaches unity, it is possible that $\varepsilon_{1,j}(E_0, \tau_F) T_{F,j}(E_0, \tau_F) > \varepsilon_{2,j}(E_0)$ because $\varepsilon_{1,j}(E_0, \tau_F)$ includes detected events that are triggered by both the transmitted ion and secondary electrons generated at the foil's exit surface. Based on equation (7), this results in $R_H > 1$ occurring over an energy range that is dependent on the foil thickness. Even when R_H is initially greater than 1, it eventually falls to 1 as $\varepsilon_{2,j}(E_0) \rightarrow 1$ with increasing energy. No overshoot is observed for O$^+$ (i.e., $R_O \leq 1$), indicating that $\varepsilon_{1,O}(E_0, \tau_F) T_{F,O}(E_0, \tau_F) \leq \varepsilon_{2,O}(E_0)$ over the entire energy range of this study.

4. Implementation

For implementation of the technique, it is critical that the ions incident on the foil-based mass separation subsystem have previously been filtered by energy-per-charge. Thus, we consider a typical ion energy-per-charge (E/q) spectrometer consisting of an electrostatic energy analyzer (ESA) in one of several standard configurations: spherical section (Bame et al., 1978, 1993), top hat (Carlson et al., 1983), or toroidal (Young et al., 1988). The ESA, through which ions pass if their energy lies within the ESA energy passband, is normally followed by an angle-resolved ion counting detector section such as an array of CEMs or an MCP detector followed by anode segments. We now show three specific implementations demonstrating how our mass discrimination technique can be used to determine the flux of H$^+$ and O$^+$ incident on such an instrument using the counts received by each detector and the laboratory-determined species-dependent response. In section 4.1, we first introduce a two-pixel, single look direction implementation. In section 4.2, we expand this implementation to five pixels with five look directions. Finally, in section 4.3 we introduce an alternative configuration—a one-pixel, one-look direction implementation.

4.1. Two-Pixel, Single-Look Direction Implementation

A simple implementation of this technique is to deploy a flight version of the apparatus shown in Figure 2 immediately following an ESA. If employing CEMs, each pixel consists of an ESA section, a foil-covered detector D1, and a second detector D2 with no foil. If the gridded or foil-covered aperture is held at voltage V_F then the energy of the ion incident on the grid/foil, E_0, is represented by $E_0 = E_\infty + qV_F$ where E_∞ is the initial ion energy and q is the ion charge. The electronics are relatively simple because the only requirement is counting incident particles in D1 and D2.

The flux of H$^+$ and O$^+$ incident on each detector is determined by comparing the total count rate measured during the time interval of one energy step in D2 without a foil, $C_2 = C_{2,H} + C_{2,O}$, and D1 with a foil, $C_1 = C_{1,H} + C_{1,O}$. In a space application, a count from H$^+$ is indistinguishable from a count generated by O$^+$, so the quantities measured are C_1 and C_2 with no direct measurement of only C_{1j} or C_{2j}. Therefore, the expressions for flux must be in terms of total count rates on each detector, C_1 and C_2, and the experimentally determined species-dependent instrument response, given by R_O and R_H (equations (8) and (10), respectively). Additionally, unlike the laboratory measurements, a plasma in space will be neither monoenergetic

**AGU
100**
ADVANCING EARTH
AND SPACE SCIENCE

Journal of Geophysical Research: Space Physics

10.1029/2019JA027138

nor collimated. For each species j, the differential energy flux φ (cm^{-2} s^{-1} sr^{-1} keV/keV) is related to the count rate C (# s^{-1}), geometric factor G (cm^2 sr keV/keV), and detection efficiency ε by

$$\varphi_j = {C_j}/{\varepsilon_j G}. \tag{12}$$

The expression for differential energy flux for hydrogen can be determined by rewriting equation (4):

$$\varphi_H(E_0, \tau_F) = \frac{C_{1,H}(E_0, \tau_F)}{GT_G\varepsilon_{1,H}(E_0, \tau_F)T_{F,H}(E_0, \tau_F)}. \tag{13}$$

In order to obtain an expression for $C_{1,H}$ (the hydrogen counts on D1) in terms of measured count rates, we express the measured counts C_1 and C_2 on detectors D_1 and D_2 as

$$C_1 = C_{1,H} + C_{1,O} \quad and \quad C_2 = C_{2,H} + C_{2,O}. \tag{14}$$

Equation (7) applied to each species results in

$$R_O = {C_{1,O}}/{C_{2,O}} \quad and \quad R_H = {C_{1,H}}/{C_{2,H}}. \tag{15}$$

Using equation (14) to solve for $C_{1,H}$ and substituting from equation (15) results in

$$\begin{aligned}
C_{1,H} &= C_1 - C_{1,O} \\
&= C_1 - R_O C_{2,O} \\
&= C_1 - R_O \left(C_2 - \frac{C_{1,H}}{R_H} \right).
\end{aligned} \tag{16}$$

Combining like terms, the hydrogen counts on D1 can be rewritten as

$$C_{1,H}(E_0, \tau_F) = \frac{C_1(E_0, \tau_F)R_H(E_0, \tau_F) - C_2(E_0)R_O(E_0, \tau_F)R_H(E_0, \tau_F)}{R_H(E_0, \tau_F) - R_O(E_0, \tau_F)}. \tag{17}$$

Substituting equation (17) into equation (13) results in an expression for the differential energy flux, shown in equation (18). A similar procedure can be followed for determining the differential energy flux for oxygen (equation (19)).

$$\varphi_H(E_0, \tau_F) = \frac{1}{GT_G\varepsilon_{2,H}} \left(\frac{C_1 - C_2 R_O}{R_H - R_O} \right) \tag{18}$$

$$\varphi_O(E_0, \tau_F) = \frac{1}{GT_G\varepsilon_{2,O}} \left(\frac{C_2 R_H - C_1}{R_H - R_O} \right) \tag{19}$$

Of particular interest is the abundance of O$^+$ relative to H$^+$, which is simply the ratio of equations (18) and (19):

$$\frac{\varphi_O}{\varphi_H} = \frac{\varepsilon_{2,H}}{\varepsilon_{2,O}} \left(\frac{C_2 R_H - C_1}{C_1 - C_2 R_O} \right) \equiv \mathbb{R} \tag{20}$$

Optimization of this mass differentiation technique occurs when the uncertainty in $\mathbb{R}$ is minimized. That uncertainty is

$$\sigma_{\mathbb{R}} = \sqrt{\left(\frac{\partial \mathbb{R}}{\partial C_1} \right)^2 C_1 + \left(\frac{\partial \mathbb{R}}{\partial C_2} \right)^2 C_2} = \left(\frac{\varepsilon_{2,H}}{\varepsilon_{2,O}} \right) \cdot \frac{(R_H - R_O)}{(C_1 - C_2 R_O)^2} \sqrt{(C_1 C_2^2 + C_2 C_1^2)} \tag{21}$$
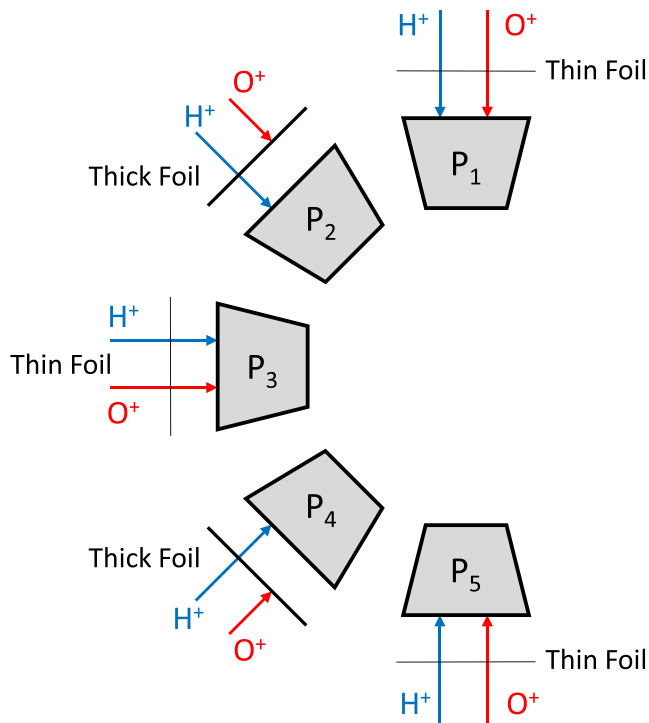
The fractional uncertainty is thus

Figure 8. A five-pixel implementation of the foil technique for separating H$^+$ and O$^+$. Pixels P$_1$, P$_3$, and P$_5$ have extremely thin foils (thinner than Foil 1 from this study). These extremely thin foils allow transmission of both H$^+$ and O$^+$. Pixels P$_2$ and P$_4$ have thicker foils (comparable to those from this study), which transmit H$^+$ and block O$^+$.

$$\frac{\sigma_{\mathbb{R}}}{\mathbb{R}} = \frac{\sqrt{C_1 C_2 (C_1 + C_2)}}{(R_{\mathrm{H}} - R_{\mathrm{O}})\varphi_{\mathrm{H}}\varphi_{\mathrm{O}}} \cdot \frac{1}{G^2 T_{\mathrm{G}}^2 \varepsilon_{2,\mathrm{H}}\varepsilon_{2,\mathrm{O}}}. \tag{22}$$

This fractional uncertainty is minimized when $R_{\mathrm{H}} - R_{\mathrm{O}}$ is maximized, which occurs when $R_{\mathrm{H}} \to 1$ (its maximum value) and $R_{\mathrm{O}} \to 0$ (its minimum value). This result is conceptually intuitive: it corresponds to a foil on D1 of sufficient thickness such that all H$^+$ is transmitted while all O$^+$ is blocked. Defining the energy passband of nominal transmission as the range over which at least 90% of H$^+$ is transmitted ($R_{\mathrm{H}} \geq 0.9$) while less than 10% of O$^+$ is transmitted ($R_{\mathrm{O}} \leq 0.1$), the foils analyzed in this study yield the widest viable energy range of ~7–24 keV for Foil 8 (Figure 6).

Differences in the detection efficiencies of detectors D1 and D2 can be further reduced by mounting an ultrathin (e.g., nominal 0.5 μg·cm^{-2}) carbon foil to the grid of detector D2. This will enhance the detection efficiency of D2 because measurement will include events triggered by both the transmitted ion and secondary electrons generated at the foil's exit surface. At this foil thickness the transmissions of both H$^+$ and O$^+$ are approximately unity (Funsten, McComas, et al., 1993), and the transmitted ions can generate secondary electrons from the backside of the foil that can be detected along with the ion (Ritzau & Baragiola, 1998). By enhancing the detection rate in D2, $\varepsilon_{2,\mathrm{H}}$ and $\varepsilon_{2,\mathrm{O}}$ both approach unity and, in particular, eliminate the overshoot $R_{\mathrm{H}} > 1$ shown in Figure 6b. Note that the arrangement described here assumes that both detectors D1 and D2 are observing flux incident from the same look direction.

4.2. A Five-Pixel Application

The implementation described in section 4.1 and shown in Figure 2 can be extended to enable measurement of H$^+$ and O$^+$ fluxes over multiple-look directions. Directional coverage can be increased by arranging a circular array of n detectors located at the output of the ESA. Figure 8 shows a five-pixel variant of this concept, where the five pixels are deployed after an ESA so that incident ions are selected for energy-per-charge (E/q). Three pixels (P$_1$, P$_3$, P$_5$) have no foil or an extremely thin foil—comparable to or thinner than Foil 1 from this study (0.83-μg·cm^{-2} calculated thickness). The two interleaved pixels (P$_2$, P$_4$) have foils with thicknesses comparable to those in Figure 6b (4–14 μg·cm^{-2}). Because each of the pixels views a different direction, plasma anisotropies must be taken into account when comparing the counts from adjacent detectors to determine the composition.

A simple assessment of the relative abundance of H$^+$ and O$^+$ as a function of azimuthal angle uses interpolation to derive composition. For example, H$^+$ and O$^+$ fluxes for an isotropic distribution can be determined using the number of counts measured in one detector (e.g., P3, measuring H$^+$ and O$^+$) and comparing with the average of the counts measured in the two adjacent detectors (e.g., P$_2$ and P$_4$, each measuring H$^+$ only). A more detailed analysis uses the measured counts in all detectors of the detector array and provides detailed information on anisotropy of the ion fluxes in addition to higher statistical accuracy of H$^+$ and O$^+$ abundances. The details of this analysis are beyond the scope of this study. The Z-Plasma Spectrometer (ZPS) is a variant of this detector concept utilizing ~0.9-μg·cm^{-2} foils for pixels P$_2$ and P$_4$ and ~10-μg·cm^{-2} foils for pixels P$_1$, P$_3$, and P$_5$. ZPS is currently aboard the National Nuclear Security Administration (NNSA) Space and Atmospheric Burst Reporting System (SABRS) payloads.

4.3. Compact Single-Pixel Implementation

Another implementation uses two detectors to derive composition in a single-look direction. Again, the foil elements are employed after an ESA so that incoming ions are already selected for energy-per-charge (E/q). An example of this concept is shown in Figure 9. In this example, D1 is covered by a grid and a thin foil, identical to D1 in Figure 2. As before, the foil covering D1 will be tuned to allow transmission of H$^+$ while blocking transmission of O$^+$. Detector D3 is covered by a grid only and is biased positive relative to the foil such that it will detect secondary electrons generated on the entrance side of the D1 foil from incident H$^+$ and O$^+$.
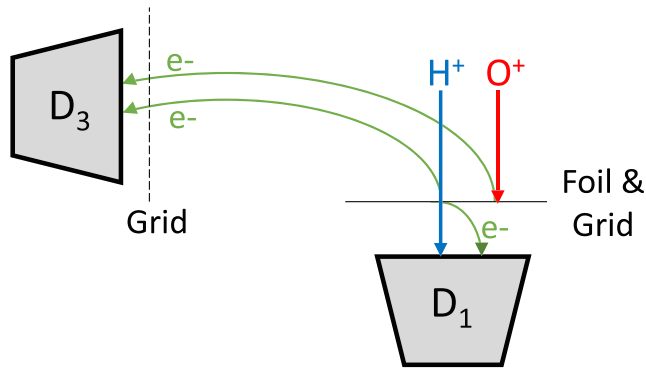
Figure 9. An implementation of the foil technique for measuring H^+ and O^+ fluxes with a single pixel. Detector D1 is covered with a grid and foil such that H^+ is transmitted while O^+ is not. Detector D3 detects secondary electrons emitted by the impact of both H^+ and O^+ on the surface of the foil.

Both H^+ and O^+ will be indirectly detected by detector D3, while detector D1 will directly detect only H^+. Therefore, comparison of the count rates between D1 and D3 enables determination of the incident H^+ and O^+ fluxes at each energy range setting of the ESA. In its lowest-resource implementation, this configuration does not require electronics for detecting coincidence; a comparison of the counts on D1 and D3 is sufficient for determining compositional abundance.

This configuration has several advantages over that shown in Figure 2. In contrast to the configuration in Figure 2 that uses two spatially separate outputs from the ESA (one for detector D1 and the other for detector D2 that each view different parts of the plasma distribution), the configuration of Figure 9 allows measurement of both H^+ and O^+ fluxes in the same look direction and thus measure the same part of the plasma distribution function. This removes the previously discussed uncertainties associated with anisotropies measured in the plasma distribution. This technique can also be useful for accurate measurement of the relative flux φ_O/φ_H if the pixel geometric factor varies as a function of the exit location of the ESA, which could be problematic for the five-pixel implementation shown in section 4.2. Additionally, with the addition of more sophisticated electronics, this configuration enables coincidence measurement in which a single H^+ can be detected in both detectors D1 and D3; in turn, this D1-D3 coincidence count rate can be compared with the count rate in detector D1 for continuous monitoring of the performance of detector D3 (described in detail below).

For the detector concept shown in Figure 9, the count rate of detector D1, C_1, is identical to that of Figure 2 and equation (4). The count rate C_3 resulting from ions impacting the foil and registering a pulse in detector D3 is

$$C_{3,j}(E_0) = A\varphi_j T_G \varepsilon_{3,j}(E_0) \tag{23}$$

where $\varepsilon_{3,j}(E_0)$ is the detection efficiency for ions of species j impacting the foil and is a convolution of the secondary electron yield distribution off the front of the foil and the probability that these secondary electrons generate a pulse in detector D3. The grid transmission T_G for the grid in front of D3, detector area A, and ion beam flux φ_j for each ion species are assumed to be the same as for detector D1.

The ratio R of count rates of the detectors D1 and D3 for a particular ion species j at incident energy E_0 is

$$R_j(E_0, \tau_F) = \frac{C_{1,j}(E_0, \tau_F)}{C_{3,j}(E_0)} = \frac{\varepsilon_{1,j}(E_0, \tau_F)}{\varepsilon_{3,j}(E_0)} T_{F,j}(E_0, \tau_F). \tag{24}$$

The value of R_j for H^+ and O^+ can be derived via laboratory measurement using an experimental apparatus and method that reproduces the configuration shown in Figure 9.

This technique can be extended to a space application, where the incident plasma distribution will be neither monoenergetic nor collimated. As before, a count from H^+ is indistinguishable from a count generated by O^+, so the quantity measured is C_1 and C_3 with no direct measurement of only $C_{1,j}$ or $C_{3,j}$. The H^+ and O^+ differential energy fluxes derived using the total count rates $C_1 = C_{1,H} + C_{1,O}$ in detector D1 and $C_3 = C_{3,H} + C_{3,O}$ in detector D3 are

$$\varphi_H(E_0, \tau_F) = \frac{1}{G T_G \varepsilon_{3,H}} \left(\frac{C_1 - C_3 R_O}{R_H - R_O} \right) \tag{25}$$

$$\varphi_O(E_0, \tau_F) = \frac{1}{G T_G \varepsilon_{3,O}} \left(\frac{C_3 R_H - C_1}{R_H - R_O} \right), \tag{26}$$

where R_H and R_O are defined in equation (24). By combining equations (25) and (26), the abundance of O^+ relative to H^+ is

$$\frac{\varphi_O}{\varphi_H} = \frac{\varepsilon_{3,H}}{\varepsilon_{3,O}}\left(\frac{C_3 R_H - C_1}{C_1 - C_3 R_O}\right). \tag{27}$$

As with the configuration shown in Figure 2, the technique for this configuration is optimized when the statistical error of the abundance ratio φ_O/φ_H is minimized. Again utilizing equations (21) and (22) for assessing the error, the technique is optimized when $R_H \to 1$ and $R_O \to 0$, corresponding to a foil of sufficient thickness so that the transmission of H^+ is 100% while the transmission of O^+ is 0%.

As mentioned above, an added benefit of the configuration shown in Figure 9 is the ability to use coincidence measurements between D1 and D3 to monitor the absolute H^+ efficiency of detector D3. This derivation of the D3 absolute detection efficiency assumes minimal noise interference, measurements of only a single particle at a time, and no random coincidence measurements between particles of different species (Funsten et al., 2005).

At low ion energies only H^+ is detected, thus $C_{1,O} = 0$ and correspondingly $R_O = 0$. The probability of detecting hydrogen using D1 is

$$P_{1,H}(E_0, \tau_F) = T_G \varepsilon_{1,H}(E_0, \tau_F) T_{F,H}(E_0, \tau_F). \tag{28}$$

The probability of detecting hydrogen using D3 is

$$P_{3,H}(E_0) = T_G \varepsilon_{3,H}(E_0). \tag{29}$$

A reasonable assumption for this method is that the factors affecting the detection efficiency of D1 are independent of those affecting measurement of secondary electrons at D3. Therefore, the probability of a coincidence between detectors D1 and D3 is simply the product of their individual detection probabilities: $P_{1,3} = P_1 P_3$. Thus, the coincidence count rate is

$$C_{1,3,H}(E_0, \tau_F) = G\varphi_H P_{1,H}(E_0, \tau_F) P_{3,H}(E_0)$$
$$= G\varphi_H T_G^2 \varepsilon_{1,H}(E_0, \tau_F) T_{F,H}(E_0, \tau_F) \varepsilon_{3,H}(E_0). \tag{30}$$

The ratio $C_{1,3,H}/C_{1,H}$ is the absolute detection probability for detector D3:

$$P_{3,absolute} = \frac{C_{1,3,H}(E_0, \tau_F)}{C_{1,H}(E_0, \tau_F)} = T_G \varepsilon_{3,H}(E_0). \tag{31}$$

Thus, monitoring the coincidence count rate between D1 and D3 enables determination of the absolute detection efficiency of D3 for incident H^+ above ~1 keV (the approximate low-energy threshold for H^+ in D1). In this way the performance of D3 can be monitored throughout the mission. Note that in the general case, this technique can only be used to determine the detection efficiency of D3 and not D1, since D1 detects only H^+ whereas D3 is sensitive to both H^+ and O^+, even at low energies. Conversely, in an environment where the measurements determine no oxygen is present ($\varphi_H \gg \varphi_O$), the detection efficiency for H^+ above ~1 keV (the approximate low-energy threshold for H^+ in D1) can be determined for both D3 and D1. Likewise, in an environment where no H^+ is present ($\varphi_O \gg \varphi_H$), the detection efficiency for O^+ above ~10 keV (the approximate low-energy threshold for O^+ in D1) can be determined for both detectors.

5. Summary

In this study we presented a novel application of ultrathin foils for low-resource mass differentiation of H^+ and O^+ for space weather applications. This instrument concept utilizes two detector configurations: configuration D2 consists of a detector with only a grid and no foil which measures incident H^+ and O^+ flux, while configuration D1 is a detector with a grid and foil that transmits H^+ and blocks O^+ through an exploitation of the difference in stopping power for incident ions of different species. To demonstrate the feasibility of this mass differentiation technique we built a concept prototype and characterized its response to monoenergetic H^+ and O^+ ion beams. We characterized eight ultrathin carbon foils, for which we first measured the

angular scatter distribution of transmitted H^+ ions as a function of energy, a proxy for the foil thickness. We then measured the transmission of H^+ and O^+ through the two detector configurations. We confirmed the following features of ultrathin foil transmission:

1. Neither H^+ nor O^+ are observed to transit a foil at very low energies because they are completely stopped in the foil.
2. The energy at which ions begin to transit a foil increases with increasing foil thickness.
3. O^+ begins to transit a foil of a particular thickness at an energy that is substantially higher than for H^+ due to the larger energy loss of O^+ in the foil relative to H^+.
4. The transmission of both H^+ and O^+ at higher energies both approach unity as more ions successfully transit the foil.

We determined that there is an upper limit of a few tens of keV for this O^+/H^+ separation technique. Over the operable energy range for this technique, the measured ratio of O^+/H^+ can range from near zero (no O^+ present, all H^+ measured) to very large (minimal H^+ present, all O^+ measured). The concept is a low-resource monitor for distinguishing O^+ and H^+; additional measurement is required to separate H^+ from He^+, or to distinguish ions within the CNO group.

We presented two implementations of this technique in a space-qualified instrument. The low-resource configuration consists of alternating D1 and D2 detector subsystems for separating measurements of H^+ and O^+. The strength of this technique is its simplicity, with the drawback resulting from different look directions for D1 and D2. A more complicated implementation employs two detectors that measure H^+ and O^+ in the same look direction, again with relatively simple electronics. Upgrading the electronics to enable coincidence measurements in this configuration yields the added benefit of continuous monitoring of the foil-free detector performance. Finally, we derived expressions for the H^+ flux and O^+ flux incident on the instrument using only the counts received by each detector and the laboratory-determined, species-dependent response—these expressions demonstrate that the instrument is capable of O^+/H^+ mass differentiation in a space plasma environment.

References

Allegrini, F., Ebert, R. W., & Funsten, H. O. (2016). Carbon foils for space plasma instrumentation. *Journal of Geophysical Research: Space Physics*, *121*, 3931–3950. https://doi.org/10.1002/2016JA022570

Allegrini, F., Ebert, R. W., Fuselier, S. A., Nicolaou, G., Bedworth, P. V., Sinton, S. W., & Trattner, K. J. (2014). Charge state of ~1 to 50 keV ions after passing through graphene and ultrathin carbon foils. *Optical Engineering*, *53*(2), 24,101–24,107. https://doi.org/10.1117/1.OE.53.2.024101

Balsiger, H. (1981). Composition of hot ions (0.1-16 keV/e) as observed by the GEOS and ISEE mass spectrometers and inferences for the origin and circulation of magnetospheric plasmas. *Advances in Space Research*, *1*(1), 289–303. https://doi.org/10.1016/0273-1177(81)90124-1

Balsiger, H., Eberhardt, P., Geiss, J., Ghielmetti, A., Walker, H. P., Young, D. T., et al. (1976). A satellite-borne ion mass spectrometer for the energy range 0 to 16 keV. *Space Science Instrumentation*, *2*, 499–521.

Bame, S. J., Asbridge, J. R., Felthauser, H. E., Glore, J. P., Paschmann, G., Hemmerich, P., et al. (1978). ISEE-1 and ISEE-2 Fast Plasma Experiment and the ISEE-1 Solar Wind Experiment. *IEEE Transactions on Geoscience Electronics*, *16*(3), 216–220. https://doi.org/10.1109/TGE.1978.294550

Bame, S. J., McComas, D. J., Thomsen, M. F., Barraclough, B. L., Elphic, R. C., Glore, J. P., et al. (1993). Magnetospheric plasma analyzer for spacecraft with constrained resources. *Review of Scientific Instruments*, *64*(4), 1026–1033. https://doi.org/10.1063/1.1144173

Banks, B. A., de Groh, K. K., & Miller, S. K. (2004). Low Earth Orbital Atomic Oxygen Interactions with Spacecraft Materials. *MRS Proceedings*, *851*, NN8.1. https://doi.org/10.1557/PROC-851-NN8.1

Banks, B. A., Rutledge, S. K., de Groh, K. K., Auer, B. M., & Hill, C. M. (1993). Atomic Oxygen Protective Coatings. In R. N. DeWitt, D. Duston, & A. K. Hyder (Eds.), *The Behavior of Systems in the Space Environment* (pp. 913–919). Dordrecht, Netherlands: Springer. https://doi.org/10.1007/978-94-011-2048-7_42

Brinza, D. E. (1993). An Overview of the Long Duration Exposure Facility: Case Studies for the Effects of the Space Environment on Spacecraft Systems. In R. N. DeWitt, D. Duston, & A. K. Hyder (Eds.), *The Behavior of Systems in the Space Environment* (pp. 655–667). Dordrecht, Netherlands: Springer. https://doi.org/10.1007/978-94-011-2048-7_26

Bürgi, A., Gonin, M., Oetliker, M., Bochsler, P., Geiss, J., Lamy, T., et al. (1993). Charge exchange of low energy ions in thin carbon foils. II. Results for ions of B, C, F, Ne, Na, Si, S, Cl, Ar, K, and Fe. *Journal of Applied Physics*, *73*(9), 4130–4139. https://doi.org/10.1063/1.352846

Carlson, C. W., Curtis, D. W., Paschmann, G., & Michael, W. (1983). An instrument for rapidly measuring plasma distribution functions with high resolution. *Advances in Space Research*, *2*(7), 67–70. https://doi.org/10.1016/0273-1177(82)90151-X

Chappell, C. R., Moore, T. E., & Waite, J. H. Jr. (1987). The Ionosphere as a Fully Adequate Source of Plasma for the Earth's Magnetosphere. *Journal of Geophysical Research*, *92*(A6), 5896–5910. https://doi.org/10.1029/JA092iA06p05896

Collin, H., Quinn, J. M., Smith, G. R., Hertzberg, E., Roselle, S., & Battel, S. J. (1992). Low-energy Ion Mass Spectrometer on CRRES. *Journal of Spacecraft and Rockets*, *29*(4), 617–620. https://doi.org/10.2514/3.25511

Craven, P. D., Olsen, R. C., Chappell, C. R., & Kakani, L. (1985). Observations of molecular ions in the Earth's magnetosphere. *Journal of Geophysical Research*, *90*(A8), 7599–7605. https://doi.org/10.1029/ja090ia08p07599

Denton, M. H., Thomsen, M. F., Korth, H., Lynch, S., Zhang, J. C., & Liemohn, M. W. (2005). Bulk plasma properties at geosynchronous orbit. *Journal of Geophysical Research*, *110*, A07223. https://doi.org/10.1029/2004JA010861

Denton, M. H., Thomsen, M. F., Reeves, G. D., Larsen, B. A., Henderson, M. G., Jordanova, V. K., et al. (2017). The Evolution of the Plasma Sheet Ion Composition: Storms and Recoveries. *Journal of Geophysical Research: Space Physics*, *122*, 12,040–12,054. https://doi.org/10.1002/2017JA024475

Ebert, R. W., Allegrini, F., Fuselier, S. A., Nicolaou, G., Bedworth, P., Sinton, S., & Trattner, K. J. (2014). Angular scattering of 1–50 keV ions through graphene and thin carbon foils: Potential applications for space plasma instrumentation. *Review of Scientific Instruments*, *85*, 033302. https://doi.org/10.1063/1.4866850

Fernandes, P. A., Larsen, B. A., Thomsen, M. F., Skoug, R. M., Reeves, G. D., Denton, M. H., et al. (2017). The plasma environment inside geostationary orbit: A Van Allen Probes HOPE survey. *Journal of Geophysical Research: Space Physics*, *122*, 9207–9227. https://doi.org/10.1002/2017JA024160

Frank, L. A., Ackerson, K. L., Paterson, W. R., Lee, J. A., English, M. R., & Pickett, G. L. (1994). The Comprehensive Plasma Instrumentation (CPI) for the GEOTAIL Spacecraft. *Journal of Geomagnetism and Geoelectricity*, *46*(1), 23–37. https://doi.org/10.5636/jgg.46.23

Fu, S. Y., Zong, Q.-G., Wilken, B., & Pu, Z. Y. (2001). Temporal and spatial variation of the ion composition in the ring current. *Space Science Reviews*, *95*(1/2), 539–554. https://doi.org/10.1023/A:1005212906199

Funsten, H. O., Allegrini, F., Bochsler, P., Dunn, G., Ellis, S., Everett, D., et al. (2009). The Interstellar Boundary Explorer High Energy (IBEX-Hi) Neutral Atom Imager. *Space Science Reviews*, *146*(1-4), 75–103. https://doi.org/10.1007/s11214-009-9504-y

Funsten, H. O., Barraclough, B. L., & McComas, D. J. (1993). Shell effects observed in exit charge state distribution of 1–30 keV atomic projectiles transiting ultrathin carbon foils. *Nuclear Instruments and Methods in Physics Research Section B: Beam Interactions with Materials and Atoms*, *80-81*, 49–52. https://doi.org/10.1016/0168-583X(93)96074-M

Funsten, H. O., Barraclough, B. L., & McComas, D. J. (1994). Interactions of slow H, H2, and H3 with thin carbon foils. *Nuclear Instruments and Methods in Physics Research B*, *90*(1–4), 24–28. https://doi.org/10.1016/0168-583X(94)95503-4

Funsten, H. O., Dors, E. E., Harper, R. W., & Reisenfeld, D. B. (2007). US 7,217,918 B1. United States. Retrieved from https://patents.google.com/patent/US7217918

Funsten, H. O., Harper, R. W., & McComas, D. J. (2005). Absolute detection efficiency of space-based ion mass spectrometers and neutral atom imagers. *Review of Scientific Instruments*, *76*, 053301. https://doi.org/10.1063/1.1889465

Funsten, H. O., McComas, D. J., & Barraclough, B. L. (1992). Thickness uniformity and pinhole density analysis of thin carbon foils using incident keV ions. *Nuclear Instruments and Methods in Physics Research B*, *66*(4), 470–478. https://doi.org/10.1016/0168-583X(92)95421-M

Funsten, H. O., McComas, D. J., & Barraclough, B. L. (1993). Ultrathin foils used for low-energy neutral atom imaging of the terrestrial magnetosphere. *Optical Engineering*, *32*, 32–36. Retrieved from https://doi.org/10.1117/12.149187

Funsten, H. O., Ritzau, S. M., Harper, R. W., Borovsky, J. E., & Johnson, R. E. (2004). Energy Loss by keV Ions in Silicon. *Physical Review Letters*, *92*, 213201. https://doi.org/10.1103/PhysRevLett.92.213201

Funsten, H. O., & Shappirio, M. (1997). Sputtering of thin carbon foils by 20 keV and 40 keV Ar+ bombardment. *Nuclear Instruments and Methods in Physics Research Section B: Beam Interactions with Materials and Atoms*, *127-128*, 905–909. https://doi.org/10.1016/S0168-583X(97)00079-7

Funsten, H. O., Skoug, R. M., Guthrie, A. A., MacDonald, E. A., Baldonado, J. R., Harper, R. W., et al. (2013). Helium, Oxygen, Proton, and Electron (HOPE) Mass Spectrometer for the Radiation Belt Storm Probes Mission. *Space Science Reviews*, *179*, 423–484. https://doi.org/10.1007/s11214-013-9968-7

Funsten, H. O., Suszcynsky, D. M., Harper, R. W., Nordholt, J. E., & Barraclough, B. L. (1996). Effect of local electric fields on microchannel plate detection of incident 20 keV protons. *Review of Scientific Instruments*, *67*(1), 145–154. https://doi.org/10.1063/1.1146562

Geiss, J., Balsiger, H., Eberhardt, P., Walker, H. P., Weber, L., Young, D. T., & Rosenbauer, H. (1979). Dynamics of Magnetospheric Ion Composition as Observed by the GEOS Mass Spectrometer. In K. Knott, A. Durney, & K. Ogilvie (Eds.), *Advances in Magnetosperic Physics with GEOS-1 and ISEE* (pp. 217–246). Dordrecht, Netherlands: Springer. https://doi.org/10.1007/978-94-009-9527-7_16

Gloeckler, G., & Hamilton, D. C. (1987). AMPTE Ion Composition Results. *Physica Scripta*, *T18*, 73–84. https://doi.org/10.1088/0031-8949/1987/T18/009

Gloeckler, G., Ipavich, F. M., Studemann, W., Wilken, B., Hamilton, D. C., Kremser, G., et al. (1985). The Charge-Energy-Mass Spectrometer for 0.3-300 keV/e Ions on the AMPTE CCE. *IEEE Transactions on Geoscience and Remote Sensing*, *GE-23*(3), 234–240. https://doi.org/10.1109/TGRS.1985.289519

Hamilton, D. C., Gloeckler, G., Ipavich, F. M., Stüdemann, W., Wilken, B., & Kremser, G. (1988). Ring current development during the great geomagnetic storm of February 1986. *Journal of Geophysical Research*, *93*(A12), 14,343–14,355. https://doi.org/10.1029/JA093iA12p14343

Jahn, J.-M., Goldstein, J., Reeves, G. D., Fernandes, P. A., Skoug, R. M., Larsen, B. A., & Spence, H. E. (2017). The Warm Plasma Composition in the Inner Magnetosphere During 2012–2015. *Journal of Geophysical Research: Space Physics*, *122*, 11,018–11,043. https://doi.org/10.1002/2017JA024183

Johnson, R. G. (1979). Energetic ion composition in the Earth's magnetosphere. *Reviews of Geophysics and Space Physics*, *17*(4), 696–4502. https://doi.org/10.1029/RG017i004p00696

Johnson, R. G., Sharp, R. D., & Shelley, E. G. (1975). Composition of the Hot Plasmas in the Magnetosphere. In B. Hultqvist & L. Stenflo (Eds.), *Physics of the Hot Plasma in the Magnetosphere* (pp. 45–68). Boston, MA: Springer US. https://doi.org/10.1007/978-1-4613-4437-7_3

Karimabadi, H., Roytershteyn, V., Mouikis, C. G., Kistler, L. M., & Daughton, W. (2011). Flushing effect in reconnection: Effects of minority species of oxygen ions. *Planetary and Space Science*, *59*(7), 526–536. https://doi.org/10.1016/j.pss.2010.07.014

Kistler, L. M., Mouikis, C., Möbius, E., Klecker, B., Sauvaud, J. A., Réme, H., et al. (2005). Contribution of nonadiabatic ions to the cross-tail current in an O+ dominated thin current sheet. *Journal of Geophysical Research*, *110*, A06213. https://doi.org/10.1029/2004JA010653

Kistler, L. M., & Mouikis, C. G. (2016). The inner magnetosphere ion composition and local time distribution over a solar cycle. *Journal of Geophysical Research: Space Physics*, *121*, 2009–2032. https://doi.org/10.1002/2015JA021883

Kistler, L. M., Mouikis, C. G., Spence, H. E., Menz, A. M., Skoug, R. M., Funsten, H. O., et al. (2016). The source of O+ in the storm time ring current. *Journal of Geophysical Research: Space Physics*, *121*, 5333–5349. https://doi.org/10.1002/2015JA022204

Koontz, S. L., Cross, J. B., Hoffbauer, M. A., & Kirkendahl, T. D. (1991). Atomic Oxygen Degradation of Intelsat 4-type Solar Array Interconnects: Laboratory Investigations. *NASA Technical Report*, *NASA-TM-10*.

Kronberg, E. A., Ashour-Abdalla, M., Iannis, D., Delcourt, D. C., Grigorenko, E. E., Kistler, L. M., et al. (2014). Circulation of heavy ions and their dynamical effects in the magnetosphere: recent observations and models. *Space Science Reviews*, *184*, 173–235. https://doi.org/10.1007/s11214-014-0104-0

Lennartsson, W. (1989). Energetic (0.1- to 16-keV/e) magnetospheric ion composition at different levels of solar F10.7. *Journal of Geophysical Research*, *94*(A4), 3600–3610. https://doi.org/10.1029/JA094iA04p03600

Lennartsson, W., & Sharp, R. D. (1982). A comparison of the 0.1-17 keV/e ion composition in the near equatorial magnetosphere between quiet and disturbed conditions. *Journal of Geophysical Research*, *87*, 6109–6120. https://doi.org/10.1029/JA087iA08p06109

Lennartsson, W., Sharp, R. D., Shelley, E. G., Johnson, R. G., & Balsiger, H. (1981). Ion composition and energy distribution during 10 magnetic storms. *Journal of Geophysical Research*, *86*(A6), 4628–4638. https://doi.org/10.1029/JA086iA06p04628

Lennartsson, W., Shelley, E. G., Sharp, R. D., Johnson, R. G., & Balsiger, H. (1979). Some initial ISEE-1 results on the ring current composition and dynamics during the magnetic storm of December 11, 1977. *Geophysical Research Letters*, *6*(6), 483–486. https://doi.org/10.1029/GL006i006p00483

MacDonald, E. A., Funsten, H. O., Dors, E. E., Thomsen, M. F., Janzen, P. H., Skoug, R. M., et al. (2009). New Magnetospheric Ion Composition Measurement Techniques. *AIP Conference Proceedings*, *1144*(1), 168–172. https://doi.org/10.1063/1.3169283

Maggiolo, R., & Kistler, L. M. (2014). Spatial variation in the plasma sheet composition: Dependence on geomagnetic and solar activity. *Journal of Geophysical Research: Space Physics*, *119*, 2836–2857. https://doi.org/10.1002/2013JA019517

Marletta, G., & Iacona, F. (1993). Heat-induced versus particle-beam-induced chemistry in polyimide. *Nuclear Instruments and Methods in Physics Research Section B: Beam Interactions with Materials and Atoms*, *80–81*, 1045–1049. https://doi.org/10.1016/0168-583X(93)90733-M

McComas, D. J., Allegrini, F., Pollock, C. J., Funsten, H. O., Ritzau, S., & Gloeckler, G. (2004). Ultrathin (~10 nm) carbon foils in space instrumentation. *Review of Scientific Instruments*, *75*(11), 4863–4870. https://doi.org/10.1063/1.1809265

McComas, D. J., Buzulukova, N., Connors, M. G., Dayeh, M. A., Goldstein, J., Funsten, H. O., et al. (2012). Two Wide-Angle Imaging Neutral-Atom Spectrometers and Interstellar Boundary Explorer energetic neutral atom imaging of the 5 April 2010 substorm. *Journal of Geophysical Research*, *117*, A03225. https://doi.org/10.1029/2011JA017273

Meyer, L. (1971). Plural and multiple scattering of low-energy heavy particles in solids. *Physica Status Solidi B*, *44*(1), 253–268. https://doi.org/10.1002/pssb.2220440127

Möbius, E., Kistler, L. M., Popecki, M. A., Crocker, K. N., Granoff, M., Jiang, Y., et al. (2013). The 3-D Plasma Distribution Function Analyzers with Time-of-Flight Mass Discrimination for Cluster, FAST, and Equator-S. In *Measurement Techniques in Space Plasmas: Particles* (pp. 243–248). Washington, DC: American Geophysical Union (AGU). https://doi.org/10.1029/GM102p0243

Moore, T. E., Chappell, C. R., Chandler, M. O., Fields, S. A., Pollock, C. J., Reasoner, D. L., et al. (1995). The Thermal Ion Dynamics Experiment and Plasma Source Instrument. *Space Science Reviews*, *71*(1-4), 409–458. https://doi.org/10.1007/BF00751337

Moore, T. E., Chornay, D. J., Collier, M. R., Herrero, F. A., Johnson, J., Johnson, M. A., et al. (2000). The Low-Energy Neutral Atom Imager for Image. In J. L. Burch (Ed.), *The Image Mission* (pp. 155–195). Dordrecht, Netherlands: Springer. https://doi.org/10.1007/978-94-011-4233-5_6

Mouikis, C. G., Kistler, L. M., Liu, Y. H., Klecker, B., Korth, A., & Dandouras, I. (2010). H+ and O+ content of the plasma sheet at 15–19 Re as a function of geomagnetic and solar activity. *Journal of Geophysical Research*, *115*, A00J16. https://doi.org/10.1029/2010JA015978

Paillous, A. (1993). Radiation Damage to Surface and Structure Materials. In R. N. DeWitt, D. Duston, & A. K. Hyder (Eds.), *The Behavior of Systems in the Space Environment* (pp. 383–405). Dordrecht, Netherlands: Springer. https://doi.org/10.1007/978-94-011-2048-7_17

Plis, E. A., Engelhart, D. P., Cooper, R., Johnston, W. R., Ferguson, D., & Hoffmann, R. (2019). Review of Radiation-Induced Effects in Polyimide. *Applied Sciences*, *9*, 1999. https://doi.org/10.3390/app9101999

Pollock, C. J., Asamura, K., Baldonado, J., Balkey, M. M., Barker, P., Burch, J. L., et al. (2000). Medium energy neutral atom (MENA) imager for the IMAGE mission. *Space Science Reviews*, *91*(1/2), 113–154. https://doi.org/10.1023/A:1005259324933

Rème, H., Bosqued, J. M., Sauvaud, J. A., Cros, A., Dandouras, J., Aoustin, C., et al. (1997). The CLUSTER Ion Spectrometry (CIS) Experiment. *Space Science Reviews*, *79*(1/2), 303–350. https://doi.org/10.1023/A:1004929816409

Ritzau, S. M., & Baragiola, R. A. (1998). Electron emission from carbon foils induced by keV ions. *Physical Review B*, *58*(5), 2529–2538. https://doi.org/10.1103/PhysRevB.58.2529

Roussel, J.-F., & Bourdon, A. (2000). Oxygen Interaction with Materials III: Data Interpretation via Computer Simulation. *Journal of Spacecraft and Rockets*, *37*(3), 324–330. https://doi.org/10.2514/2.3582

Seki, K., Keika, K., Kasahara, S., Yokota, S., Hori, T., Asamura, K., et al. (2019). Statistical properties of molecular ions in the ring current observed by the Arase (ERG) satellite. *Geophysical Research Letters*, *46*, 8643–8651. https://doi.org/10.1029/2019gl084163

Shelley, E. G., Johnson, R. G., & Sharp, R. D. (1972). Satellite observations of energetic heavy ions during a geomagnetic storm. *Journal of Geophysical Research*, *77*(31), 6104–6110. https://doi.org/10.1029/JA077i031p06104

Shelley, E. G., Sharp, R. D., Johnson, R. G., Geiss, J., Eberhardt, P., Balsiger, H., et al. (1978). Plasma composition experiment on ISEE-A. *IEEE Transactions on Geoscience Electronics*, *16*(3), 266–270. https://doi.org/10.1109/TGE.1978.294560

Spence, H. E., Reeves, G. D., Baker, D. N., Blake, J. B., Bolton, M., Bourdarie, S., et al. (2013). Science Goals and Overview of the Radiation Belt Storm Probes (RBSP) Energetic Particle, Composition, and Thermal Plasma (ECT) Suite on NASA's Van Allen Probes Mission. *Space Science Reviews*, *179*, 311–336. https://doi.org/10.1007/s11214-013-0007-5

Tahara, H., Zhang, L., Hiramatsu, M., Yasui, T., Yoshikawa, T., Setsuhara, Y., & Miyake, S. (1995). Exposure of space material insulators to energetic ions. *Journal of Applied Physics*, *78*(6), 3719–3723. https://doi.org/10.1063/1.359951

Tennyson, R. C. (1993). Atomic Oxygen and Its Effect on Materials. In R. N. DeWitt, D. Duston, & A. K. Hyder (Eds.), *The Behavior of Systems in the Space Environment* (pp. 233–257). Dordrecht, Netherlands: Springer. https://doi.org/10.1007/978-94-011-2048-7_10

Visentine, J., Kinard, W., Brinker, D., Banks, B., & Albyn, K. (2002). Mir Solar-Array Return Experiment: Power Performance Measurements and Molecular Contamination Analysis Results. *Journal of Spacecraft and Rockets*, *39*(2), 187–193. https://doi.org/10.2514/2.3818

Wüest, M. (1998). Time-of-Flight Ion Composition Measurement Technique for Space Plasmas. In Measurement Techniques in Space Plasmas: Particles (pp. 141–155). Washington, DC: American Geophysical Union (AGU). https://doi.org/10.1029/GM102p0141

Wygant, J. R., Cattell, C. A., Lysak, R., Song, Y., Dombeck, J., McFadden, J., et al. (2005). Cluster observations of an intense normal component of the electric field at a thin reconnecting current sheet in the tail and its role in the shock-like acceleration of the ion fluid into the separatrix region. *Journal of Geophysical Research*, *110*, A09206. https://doi.org/10.1029/2004JA010708

Young, D. T. (1983). Near-equatorial magnetospheric particles from ~1 eV to ~1 MeV. *Reviews of Geophysics*, *21*(2), 402. https://doi.org/10.1029/RG021i002p00402

Young, D. T. (1998). Space plasma particle instrumentation and the new paradigm: Faster, cheaper, better. In R. F. Pfaff, J. E. Borovsky, & D. T. Young (Eds.), *Measurement Techniques in Space Plasmas: Particles* (pp. 1–18). Washington, DC: American Geophysical Union. https://doi.org/10.1029/GM102p0001

Young, D. T., Balsiger, H., & Geiss, J. (1982). Correlations of magnetospheric ion composition with geomagnetic and solar activity. *Journal of Geophysical Research*, *87*(A11), 9077. https://doi.org/10.1029/JA087iA11p09077

Young, D. T., Bame, S. J., Thomsen, M. F., Martin, R. H., Burch, J. L., Marshall, J. A., & Reinhard, B. (1988). 2Π-radian field-of-view toroidal electrostatic analyzer. *Review of Scientific Instruments*, *59*(5), 743–751. https://doi.org/10.1063/1.1139821

Young, D. T., Barraclough, B. L., McComas, D. J., Thomsen, M. F., McCabe, K., & Vigil, R. (1992). CRRES Low-Energy Magnetospheric Ion Composition Sensor. *Journal of Spacecraft and Rockets*, *29*(4), 596–598. https://doi.org/10.2514/3.25505

Young, D. T., Burch, J. L., Gomez, R. G., De Los Santos, A., Miller, G. P., Wilson, P. I. V., et al. (2014). Hot Plasma Composition Analyzer for the Magnetospheric Multiscale Mission. *Space Science Reviews*, *199*, 407–470. https://doi.org/10.1007/s11214-014-0119-6

Young, D. T., Geiss, J., Balsiger, H., Eberhardt, P., Ghielmetti, A., & Rosenbauer, H. (1977). Discovery of He2+ and O2+ ions of terrestrial origin in the outer magnetosphere. *Geophysical Research Letters*, *4*(12), 561–564. https://doi.org/10.1029/GL004i012p00561

Ziegler, J. F., & Biersack, J. P. (1985). The Stopping and Range of Ions in Matter. In D. A. Bromley (Ed.), *Treatise on Heavy-Ion Science: Volume 6: Astrophysics, Chemistry, and Condensed Matter* (pp. 93–129). Boston, MA: Springer US. https://doi.org/10.1007/978-1-4615-8103-1_3